JOURNAL OF ENVIRONMENTAL SCIENCES 111 (2022) 282–291

Available online at www.sciencedirect.com

ScienceDirect

www.elsevier.com/locate/jes

JOURNAL OF ENVIRONMENTAL SCIENCES

www.jesc.ac.cn

Nitrogen-enriched micro-mesoporous carbon derived from polymers organic frameworks for high-performance capacitive deionization

Jianpei Zhang[1], *Xun-an Ning*[1,*], *Danping Li*[2,*], *Yi Wang*[1], *Xiaojun Lai*[1], *Weixuan Ou*[1]

[1] *Guangzhou Key Laboratory of Environmental Catalysis and Pollution Control, School of Environment Science and Engineering, Institute of Environmental Health and Pollution Control, Guangdong University of Technology, Guangzhou 510006, China*

[2] *School of Land Resources and Environment, Key Laboratory of Agricultural Resource and Ecology in the Poyang Lake Basin of Jiangxi Province, Jiangxi Agricultural University, Nanchang 330045, China*

ARTICLE INFO

Article history:
Received 3 January 2021
Revised 7 March 2021
Accepted 8 March 2021
Available online 16 April 2021

Keywords:
Polymers organic frameworks
Nitrogen-doped carbon
Micro-mesoporous Carbon
Capacitive deionization

ABSTRACT

Nitrogenization is an effective method for improving the capacitive deionization (CDI) performance of porous carbon materials. In particular, polymer organic frameworks with heteroatom doping, containing an ordered pore structure and excellent electrochemical stability, are ideal precursors for carbon materials for high-performance CDI. In this study, a nitrogen-enriched micro-mesoporous carbon (NMC) electrode was fabricated by carbonizing a Schiff base network-1 at 500, 600, and 700 °C. Scanning electron microscopy, Fourier transform infrared spectroscopy, X-ray diffraction, N_2 adsorption-desorption, the contact angle of water, cyclic voltammetry, and electrochemical impedance spectroscopy were used to characterize the morphological structure, wettability, Brunauer–Emmett–Teller surface areas, and electrochemical performance of the NMCs. The results showed that the NMC carbonized at 600°C achieved the best specific capacitance (152.33 F/g), as well as a high electrosorption capacity (25.53 mg/g) because of its chemical composition (15.57% N) and surface area (312 m^2/g). These findings prove that NMC is viable as an electrode material for desalination by high-performance CDI applications.

Introduction

Population growth, industrial and agricultural development, and climate change have caused a rapid increase in the consumption of clean freshwater, resulting in a global shortage. Desalination technologies, such as distillation, reverse osmosis, and electrodialysis, are attracting increasing attention for the utilization of brackish water to produce freshwater. However, there are some shortcomings to these processes, such as low efficiency and severe environmental pollution (Semiat, 2008). With advantages including low cost and excellent regeneration stability, capacitive deionization (CDI) has been rapidly developed in recent years (Pastushok et al.,

---

[*] Corresponding authors.
E-mails: ningxunan666@126.com (X.-a. Ning), ldp1231@126.com (D. Li).

https://doi.org/10.1016/j.jes.2021.03.006

2019). This process consists of ions in a solution being adsorbed onto electrodes when a voltage is applied, and as the charge is removed or reversed, they are released from the electrodes (Anderson et al., 2010).

Electrode materials play a vital role in CDI performance. An ideal electrode for CDI should have the following features: high specific surface area, high conductivity, proper porous structure, and good wettability. Because carbon-based materials, such as graphene (Wei et al., 2016), carbon nanotubes (Zhu et al., 2018), activated carbon, and their composites (Singh et al., 2020), meet most of these criteria, they are the most widely used CDI electrodes. However, these materials have some severe defects, such as low utilization of specific surface area and unideal wettability, which limit the development of CDI. Therefore, it is necessary to identify new materials with excellent physical and chemical properties. Many efforts have been focused on manufacturing high-performance carbon materials to solve these problems. Mesoporous carbons have larger apertures for ion transport because their accessible surface area is larger than that of microporous carbons. Yeh et al. used a two-stage method to synthesize activated carbon electrodes from coconut shells to show that electrodes with meso-porosity exhibited a good capacitive performance. In addition, doping with nitrogen can simultaneously enhance the conductivity and wettability as it induces a large number of defects that are convenient for electron transfer and provide pseudo-capacitance rises from Faradic redox reactions. However, the high manufacturing cost, complex preparation process, and low amount of nitrogen (3%–8%) limit the performance and further application of these materials (Song et al., 2020; Wang et al., 2016). Therefore, research on nitrogen-rich mesoporous electrode materials with excellent CDI performance is extremely desirable. Furthermore, composition and structure are the major factors influencing CDI performance. Thus, the balance between nitrogen doping and pore structure should be further explored.

Polymer organic frameworks (POFs), which are constructed using light elements with strong covalent bonds, possess controllable pore sizes and good chemical and thermal stability. Carbon materials derived from POFs are used for catalysis, adsorption, gas storage and separation, and energy storage (Wang et al., 2015). Melamine is an ideal precursor for the fabrication of an organic framework because it possesses a triazine ring with three reactive amino groups. Furthermore, its high nitrogen content could provide the resulting polymers with special features. Zhao et al. studied melamine-based POFs synthesized using a solvothermal method with aromatic dialdehydes and melamine as the monomers, and found that it possessed a porous structure with a broad pore size distribution, high surface area, and high nitrogen content, making it an ideal precursor for carbon materials. Thus, POFs and their derived carbon materials are emerging as potential electrode materials for CDI. However, few studies have evaluated nitrogen-enriched micro-mesoporous carbons (NMC) derived from POFs.

Therefore, in this study, we prepared an NMC derived from a Schiff-base network-1 (SNW-1) as an enhanced performance CDI electrode. The SNW-1 is a POF with a micro-mesoporous structure and high nitrogen content, and is directly prepared using melamine and terephthalaldehyde as monomers. Therefore, the SNW-1 was selected as a precursor to prepare the NMCs and investigate the balance between pore structure and nitrogen doping in an NMC.

1. Experimental

1.1. *Materials*

Melamine (99%), terephthalaldehyde (99%), $ZnCl_2$, and polyvinylidene fluoride were obtained from the Aladdin Industrial Corporation (China). In addition, HCl, carbon black, N,N-dimethylacetamide, and NaCl were obtained from Sinopharm Chemical Reagent Co., Ltd. (China). Meanwhile, dichloromethane (99.5%), acetone (99.5%), and DMSO (99%) were obtained from the Grion Environment Technology Co., Ltd. (China).

1.2. *Characterization*

Transmission electron microscopy (TEM, FEI Talos F200S) and scanning electron microscopy (SEM, Zeiss Sigma 300) were used to measure the morphologies of the SNW-1 and NMC materials. Fourier transform infrared spectroscopy (FT-IR, Nicolet 670) was performed in the range of 500–4000 cm^{-1}. Powder X-ray diffraction (Empyrean, PANalytical B.V.) data were collected using a flat sample holder and Cu $K\alpha$ radiation at 40 kV in the 2θ range of 10–80°. X-ray photoelectron spectroscopy (XPS, ESCALAB250Xi, Thermo Fisher Scientific) was performed using a K-alpha system with Al $K\alpha$ (1486.6 eV) radiation to measure the chemical composition of the samples. Nitrogen adsorption/desorption isotherms were obtained using an ASAP 2460 (Micromeritics). The Brunauer–Emmett–Teller (BET) method was employed to measure the specific surface area (SSA), and Barrett–Joyner–Halenda models were used to calculate the pore volume and pore size distribution. The surface wettability of the samples was studied using a contact angle analysis (KRUSS DSA100) method with a drop shape analysis system. A CHI 660E electrochemical workstation was used to characterize the electrochemical performance by conducting cyclic voltammetry (CV), galvanostatic charge-discharge (GCD), and electrochemical impedance spectroscopy (EIS) in a 1 mol/L NaCl solution using a three-electrode system, which consists of a work electrode, reference electrode (Ag/AgCl, saturated 1 mol/L KCl), and counter electrode (1 $cm^2 \times 1$ cm^2 Pt slice).

1.3. *Preparation of NMC samples*

First, 0.47 g of melamine (3.73 mmol) and 0.75 g of terephthalaldehyde (5.59 mmol) were dissolved in DMSO (23 mL) and then decanted into a Teflon-lined autoclave (100 mL capacity). The mixture was heated at 180 °C for 10 h, and then washed with excess acetone and dichloromethane after cooling to approximately 30 °C. The obtained white powder was then dried under a vacuum at 30 °C for 10 hr.

The SNW-1 sample (80 mg) was transferred to ceramic boats and placed inside a temperature-programmed furnace under an argon atmosphere, wherein it was heated from room temperature to 500, 600, or 700 °C at a rate of 5 °C/min, and then maintained at the specified temperature for 2 hr before cooling to room temperature. The resultant samples were washed with deionized water and dried at 80 °C for 12 hr to obtain the NMC samples.

1.4. CDI tests

The work electrodes were fabricated and then assembled for the CDI apparatus to evaluate the desalination performance, in accordance with our previous work (Liu et al., 2019). The test electrolyte was an NaCl solution (500 mg/L), and the voltage was set at 0.8 1.0, or 1.2 V. The flow rate was set to 10 r/min during the experiment.

The desalination capacity (SAC, mg/g) was calculated using the following Eq. (1) (Li et al., 2019):

$$\mathrm{SAC} = \frac{(C_0 - C_e) \times V}{m} \tag{1}$$

where C_0 (mg/L) is the initial concentration of the NaCl solution, C_e (mg/L) is the final concentration of the NaCl solution, V (L) is the volume of the NaCl solution, and m (g) is the mass of the electrode.

The desalination rate (SAR, mg/g/min) was calculated as Eq. (2) (Li et al., 2019):

$$\mathrm{SAR} = \frac{(C_0 - C_e) \times V}{t} \tag{2}$$

where t (min) is the desalination time.

Energy consumption (W, kWh/kg) was calculated using Eq. (3) (Ma et al., 2020):

$$W = \frac{\int i \times v\mathrm{d}t}{3.6 \times (C_0 - C_e) \times V} \tag{3}$$

where i (A) is the current, v (V) is the voltage.

Finally, the charge efficiency (CE, %) was calculated as Eq. (4):

$$\mathrm{CE} = \frac{F \times V \times (C_0 - C_e)}{\int I\mathrm{d}t} \times 100\% \tag{4}$$

where, F is the Faraday constant (96,485 C/mol), and I (A) is the current.

2. Results and discussion

2.1. Characterization

The SNW-1 nanoparticles were constructed using melamine and terephthalaldehyde (Scheme 1). Fig. 1a shows the FT-IR results of SNW-1, melamine, and terephthalaldehyde, and Fig. 1b shows the XRD results of SNW-1. After the synthesis process, the SNW-1 spectrum showed no bands at 3468 cm^{-1}, 3417 cm^{-1}, 1650 cm^{-1} (H-N-H stretching) or 1683 cm^{-1} (C=O stretching), confirming that the reaction was complete (Zhao and Yan, 2015). Meanwhile, the bands located at 1471 cm^{-1} and 1539 cm^{-1} (C=N stretching) indicate that melamine was incorporated into the SNW-1 (Kim et al., 2018). As shown in Fig. 1b, the broad XRD peak in the 2θ range of 15–40° indicates that SNW-1 has amorphous characteristics with a low degree of crystallinity, which is in good agreement with previously reported literature (Shunmughanathan et al., 2015). According to the TGA results (Appendix A Fig. S1), the SNW-1 began to decompose when the temperature was greater than 30°C and completely decomposed below 900°C. Because a higher temperature causes a lower carbon yield and improves the carbonization degree of the final material, the carbonization temperatures in the experiment were set to 500, 600, and 700 °C, in which the corresponding samples were labeled as NMC500, NMC600, and NMC700, respectively.

Fig. 2a, b, e, and f show the SEM results of SNW-1, NMC500, NMC600, and NMC700, respectively, and reveal the occurrence of rough surfaces and irregular morphology at low magnification. The SNW-1 exhibits a cluster-like structure with an interconnection of many nanoparticles, which form numerous pores at the macro- and meso-scales. Further, it is clear that shrinkage occurred during the pyrolysis process, leading to reconnections among these nanoparticles and developing an interconnected network structure of micro- and meso-pores. This could be attributed to the incomplete interspace pores, which were produced during the carbonization step, as well as the structure collapse during the nanoparticle shrinkage during carbonization. The presence of these interspace pores

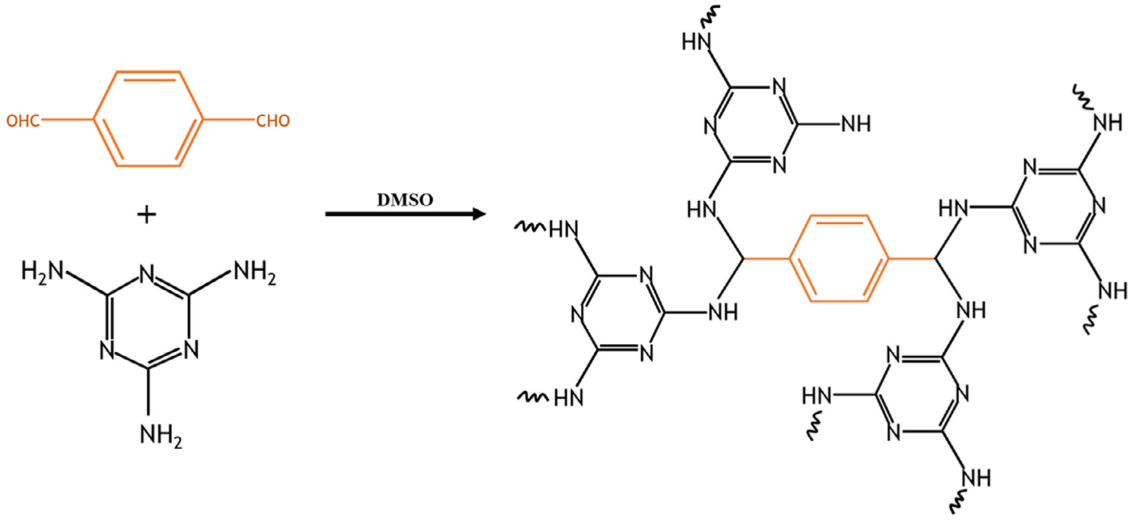

Scheme 1.

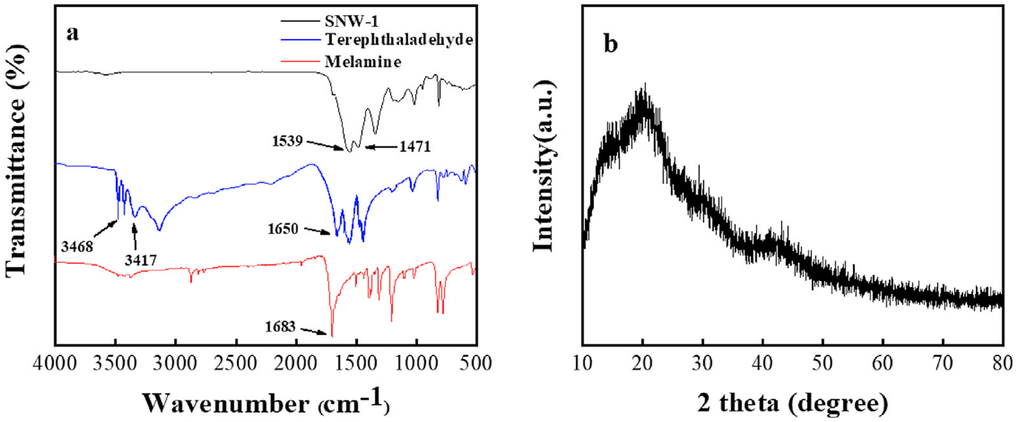

Fig. 1 – (a) FTIR spectroscopy of SNW-1, melamine, and terephthalaldehyde, (b) XRD pattern of SNW-1

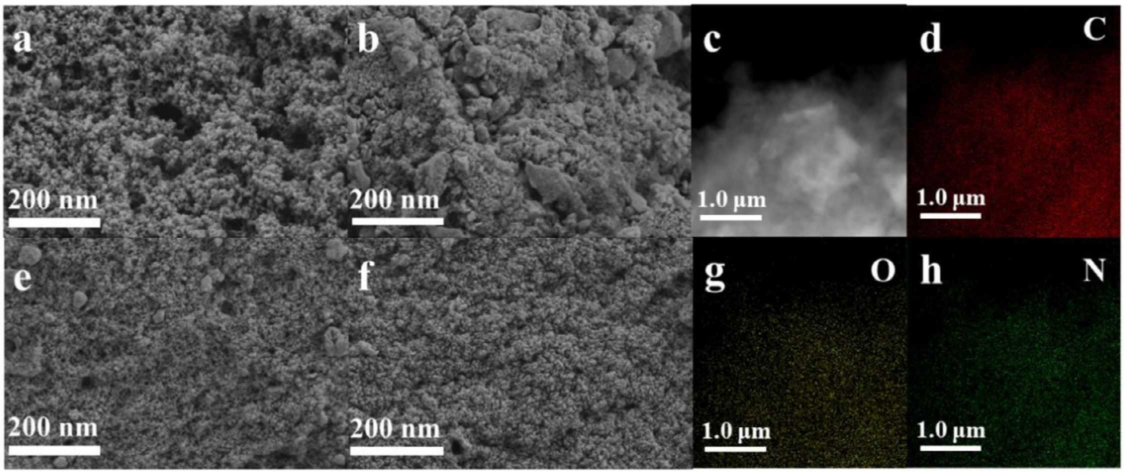

Fig. 2 – SEM images of (a) SNW-1, (b) NMC500, (e) NMC600, and (f) NMC700, (c) TEM image of NMC600, (d) C, (g) O, and (h) N element mapping of NMC600

improves ion diffusion within the structure. In addition, the TEM mapping images reveal that C, O, and N exist on the surface of the NMC600 (Fig. 2 c, d, g, and h).

Fig. 3a shows the XRD results for NMC500, NMC600, and NMC700. After carbonization, the obtained NMC showed two peaks at 2θ values of 24° and 43°. These peaks correspond to diffraction at (002) and (100), respectively, revealing the formation of partial graphitic structures. Further, with increasing temperature, the degree of graphitization increased. Fig. 3b shows the Raman spectra of NMC500, NMC600, and NMC700. In the Raman spectra, the D band at approximately 1330 cm^{-1} represents a defect within the graphitic structure and the existence of heteroatoms. Meanwhile, the G band at approximately 1590 cm^{-1} indicates E_{2g} vibration within the graphite sheet. The I_D/I_G values of NMC500, NMC600, and NMC700 were calculated to be 1.19, 1.28, and 1.32, respectively. These results demonstrate that the NMC has a disordered structure, and the degree of graphitization increases with increasing temperature. Electrical conductivity is vital for carbon materials to attain high performance in CDI, and a higher degree of graphitization implies better electrical conductivity.

The surface area results are shown in Fig. 4a. The samples displayed type I isotherms with a dramatic increase in low pressure, revealing the existence of micropores. Simultaneously, hysteresis loops at high pressures ($0.45 < P/P_0$) revealed the existence of meso-and macropores in the NMC samples. As listed in Appendix A Table S1, the SSAs and pore volumes of the NMC materials increased with increasing carbonization temperature. This may be attributed to the shrinkage and collapse of the pore structure, which is consistent with the SEM results. These results are supported by the pore size distribution shown in Fig. 4b. The average pore diameters of NMC500, NMC600, and NMC700 were 4.31 nm, 2.94 nm, and 2.55 nm, respectively. Meanwhile, the pore volume decreased in the following order: NMC700 (0.56 cm^3/g) > NMC600 (0.49 cm^3/g) > NMC500 (0.33 cm^3/g). With a large average pore size and multilevel pore structure, NMC could be a high-capacity electrode material for CDI.

As shown in Fig. 5a–c, the XPS spectra of all the NMC samples have three peaks at 285, 398, and 534 eV, indicating the existence of C, N, and O, respectively. These results suggest that they converted to nitrogen-doped carbon materials and are consistent with the XRD and Raman analyses. The atomic contents are listed in Table 1. Specifically, the N contents of NMC500, NMC600, and NMC700 were 18.58%, 15.57%, and 10.74%, respectively. Because of the decomposition of er-

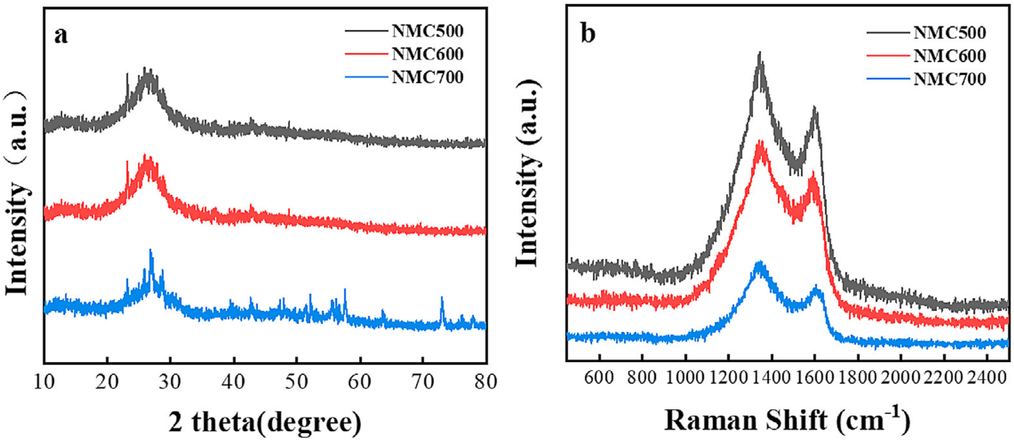

Fig. 3 – (a) XRD pattern of NMC500, NMC600, and NMC700, (b) Raman spectra of NMC500, NMC 600, and NMC 700

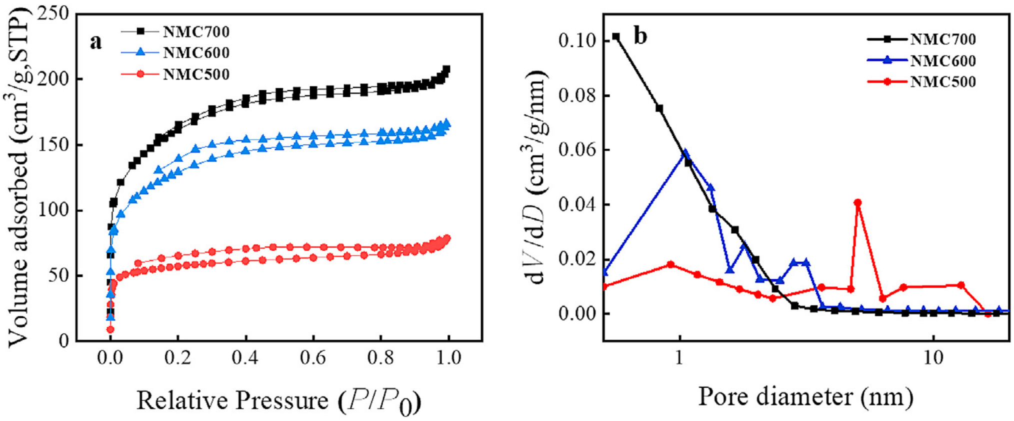

Fig 4 – (a) Nitrogen adsorption–desorption isotherms of NMC500, NMC600, and NMC700 and (b) pore size distributions of NMC500, NMC600, and NMC700

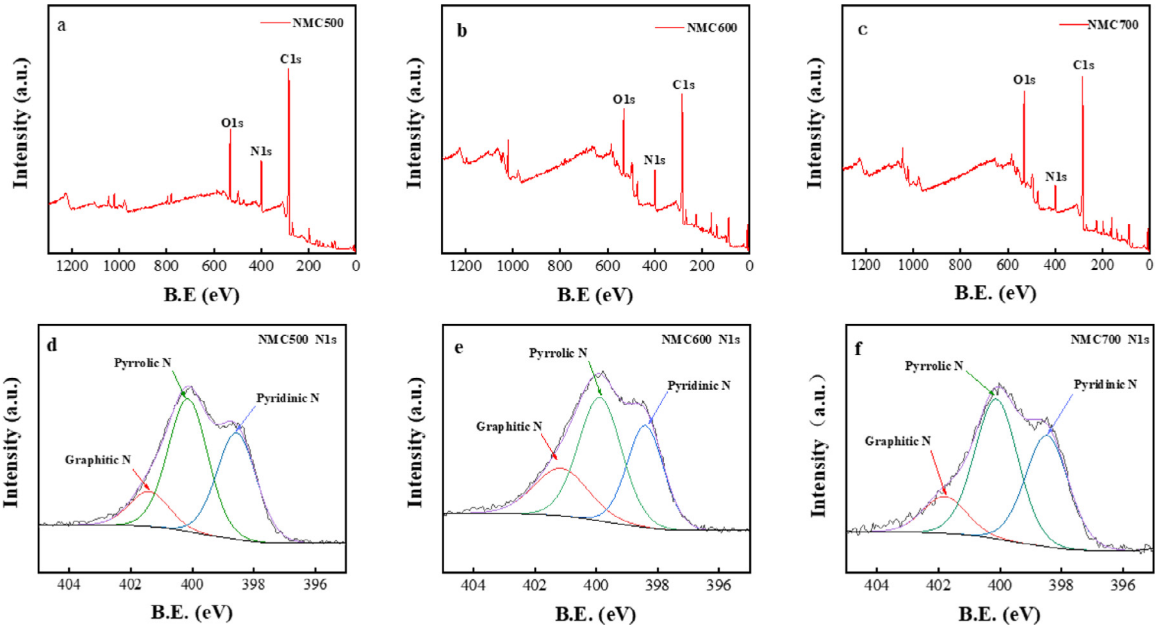

Fig. 5 – (a–c) X-ray photoelectron spectroscopy (XPS) of NMC500, NMC 600, and NMC700, and (d–e) high-resolution N1s spectrum of NMC500, NMC 600, and NMC700.

Table 1 – Elemental analysis of NMC500, NMC 600, and NMC700 by XPS.

Sample	C (%)	N (%)	O (%)	pyridinic-N (%)	pyrrolic-N (%)	graphitic-N (%)
NMC500	69.8	18.58	11.62	38.80	48.40	12.80
NMC600	70.65	15.57	13.78	38.61	48.54	12.85
NMC700	71.96	10.74	17.3	46.11	39.20	14.69

rant non-carbon elements, the C content increased while the N content decreased with increasing carbonization temperature. The high-resolution N 1s XPS spectra of the NMCs can be deconvoluted into pyridinic-N (398.3 ± 0.2 eV), pyrrolic-N (399.9 ± 0.2 eV), and graphitic N (401.0 ± 0.2 eV) (Fig. 5d and e). As shown in Appendix A Fig. S2, the C 1s spectra of the NMCs consist of three peaks, the –C–O bond at 288.3 ± 0.3 eV, the C–N bond at 286.8 ± 0.3 eV and the C–C/C = C bond at 284.6 ± 0.3 eV. Note that the peak at 288.3 ± 0.3 eV signifies N-atom existence.

To evaluate the wettability, contact angle tests of NMC500, NMC600, and NMC700 were conducted, as shown in Fig. 6. When the water contact angle is greater than 90°, the surface of the material is hydrophobic whereas when the angle is less than 90°, it is hydrophilic. According to the results, the contact angles of NMC500, NMC600, and NMC700 were 65.45°, 69.20°, and 76.35°, respectively, indicating that the NMCs are hydrophilic carbon materials. This may be because of their high nitrogen content. In addition, the wettability decreased in the order of NMC500 > NMC600 > NMC700, which may be attributed to the loss of nitrogen content with increasing carbonization temperature. The wettability results were consistent with the XPS results. Note that the solid-liquid interfacial tension may increase around the nanopores if it is hydrophobic, thereby making the nanopores inaccessible to aqueous solutions.

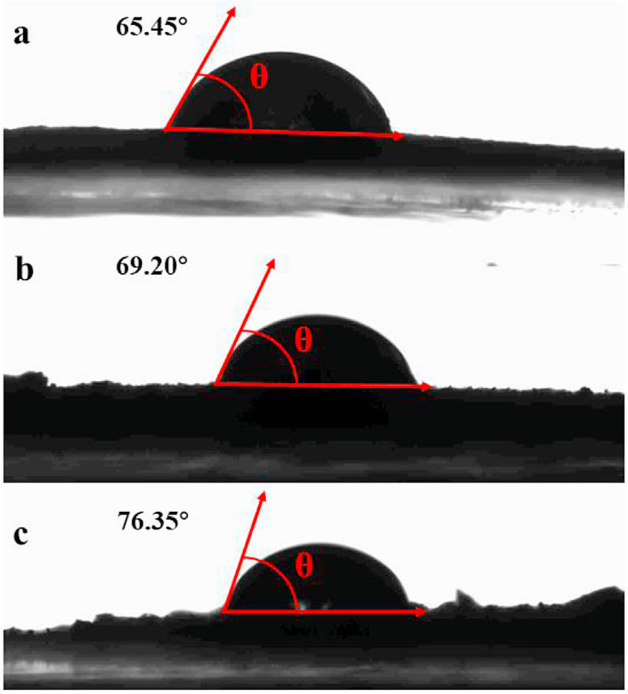

Fig. 6 – Water contact angles of (a) NMC500, (b) NMC600, and (c) NMC700.

2.2. *Electrochemical performance*

The electrochemical performances of NMC500, NMC600, and NMC700 were assessed using CV, GCD, and EIS tests. The test potential ranged from −0.5 to 0.5 V with a series of scan rates (υ, 1–100 mV/sec). The representative CV curves of NMC500, NMC600, and NMC700 at a scan rate of 10 mV/sec are shown in Fig. 7a. The rectangular CV curves indicate that the electrical double-layer capacitive behavior of the NMC electrodes was generated from a Coulombic reaction instead of a Faradic reaction (Zhao et al., 2016). In addition, a distinct deviation from the rectangle curve shape, attributable to the pseudocapacitance caused by N atoms, was also observed (Shi et al., 2020). The airtight area of the NMC600 was slightly larger than that of the NMC500 and NMC700. The specific capacitances at 1 mV/sec of the NMC500, NMC600, and NMC700 were 143.35, 152.33, and 132.4 F/g, respectively. In particular, the NMC600 had a very high electrochemical capacity. Fig. 7b shows the CV curves of NMC600 at different scan rates of 1, 10, 50, and 100 mV/sec. With increasing scan rate, the polarization effect and inherent internal resistance of the electrodes caused a deviation from the typical rectangular shape. Fig. 7c shows the specific capacitances of the NMC electrodes at different scan rates, of which the NMC600 electrode exhibited the highest specific capacitance. The BET surface area and pore volume increase made additional adsorption sites available for the ions with increasing carbonization temperature. Although the N content decreased with increasing carbonization temperature, NMC600 maintained a high nitrogen content (15.57%), thereby improving the wettability and specific capacitance. Moreover, the high degree of graphitization and multilevel pore structure provide high conductivity and an increased number of accessible pores for ion adsorption. Above all, the chemical composition and porous structure synergistically promote electrochemical performance. Although the NMC700 possesses the largest BET surface area and pore volume, its specific capacitance is lower than that of NMC600. This, which may be attributed to the high surface tension caused by the intense hydrophobic property, makes the micropores inaccessible to the electrolyte. These “dead pores” limit the electrode’s electrochemical performance. Therefore, finding a balance between the chemical composition and structure is more important than prioritizing one property as a very high electrochemical performance can be achieved with the

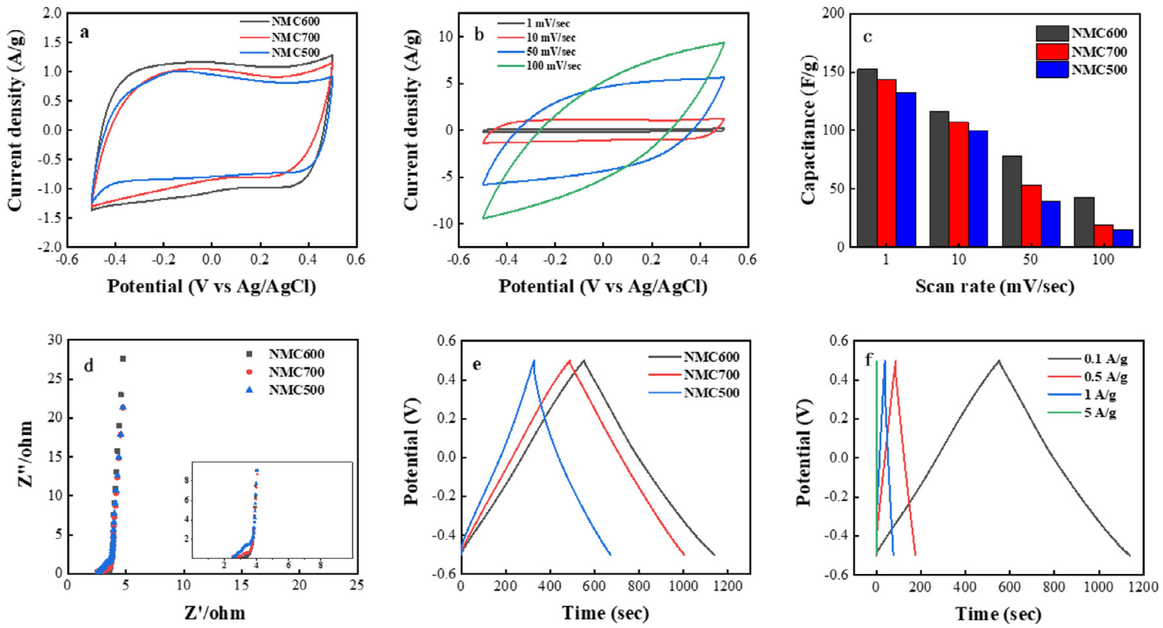

Fig. 7 – (a) CV curves at a scan rate of 10 mV/sec of NMC500, NMC 600, and NMC700, (b) CV curves of NMC600 at different scan rates, (c) the specific capacitances of NMC500, NMC 600, and NMC700 at different scan rates, (d) Comparison of EIS curves of NMC500, NMC 600, and NMC700, (e) GCD curves of NMC500, NMC 600, and NMC700, (f) GCD curves of NMC 600 at various current densities

appropriate structure and suitable chemical composition. In this study, the NMC600 provided the best results.

To distinguish the pseudocapacitive contributions. We calculated the pseudocapacitive contributions using Eqs. (5) and (6):

$$i(V) = k1\upsilon + k2\upsilon^{1/2}, \tag{5}$$

$$i(V)/\upsilon^{1/2} = k1\upsilon^{1/2} + k2, \tag{6}$$

where k_1 and k_2 are adjustable parameters that change with the applied voltage, and $i(V)$, k_1v, k_2v$^{1/2}$, and υ represent the current at a fixed voltage, the capacitive and diffusion-controlled currents, and the scan rate, respectively. As shown in Appendix A Fig. S4, the calculated capacitance/faradaic contribution of NMC600 is 48.96%/51.04%, suggesting that nitrogen induced a pseudocapacitance, which increased the CDI performance. This pseudocapacitance resulted from a reaction between the nitrogen functional groups and sodium ions, in which the pyridinic-N and pyrrolic-N species (Lewis base) of NMC600 with a strong π delocalization capture sodium ion (Lewis acid) via the acid-base interaction principle.

The results of the EIS are shown in Fig. 7d, wherein the scan frequency ranged from 10^{-2} to 10^5 Hz. The NMC500 had lowest charge-transfer resistance (R_{ct}) value (Appendix A Table S2), which is mainly attributed to its high nitrogen content. The low R_{ct} and low-frequency plots correspond to the fast ion-diffusion process inside carbon. As shown in Fig. 7e, the linear and symmetric GCD curves of NMC500, NMC600, and NMC700 indicate the electrodes all had excellent stability. In addition, NMC600 exhibited the longest charge–discharge time, suggesting that it possessed the best specific capacitance.

2.3. *CDI performance*

The desalination performance of the NMC500, NMC600, and NMC700 electrodes was tested in a 100 mL NaCl solution with an initial concentration of 500 mg/L at 1.2 V and a flow rate of 10 r/min in batch mode. As shown in Appendix A Fig. S3, the solution concentrations for all the electrodes decreased significantly, which can be attributed to the fast adsorption of ions by the electric force. With increasing time, the curves stabilized at 472.6, 469.26, and 474.44 mg/L, respectively, indicating that the salt adsorption of the electrodes reached saturation. The electrosorption capacities of the NMC500, NMC600, and NMC700 electrodes were 15.89, 25.53, and 20.15 mg/g (Fig. 8a). The electrosorption adsorption rate (SAR) is also a crucial factor for evaluating the CDI performance. The electrosorption rate of the NMC600 electrode was 1.91 mg/g/min, which is higher than that of the NMC500 (0.88 mg/g/min) and NMC700 (1.09 mg/g/min) electrodes (Fig. 8b). The position of the NMC600 electrode at the top-right of the CDI Ragone plot indicates it has the highest SAC, which can be attributed to the specific pore structure and chemical composition ratio, as well as the high degree of graphitization and high conductivity. Compared with the NMC700 electrode, the NMC600 had a higher mesopore volume and higher N content, which makes it a better salt-ion reservoir, and the coexistence of meso- and micropores ensures a better electrochemical performance. This result is in accordance with the electrochemical measurements. Although the NMC500 electrode has a lower impedance and higher N content than the NMC600 electrode, the specific area of the NMC600 electrodes is much larger. Therefore, the presence of a reasonable mesopore structure resulting in a highly accessible surface area and

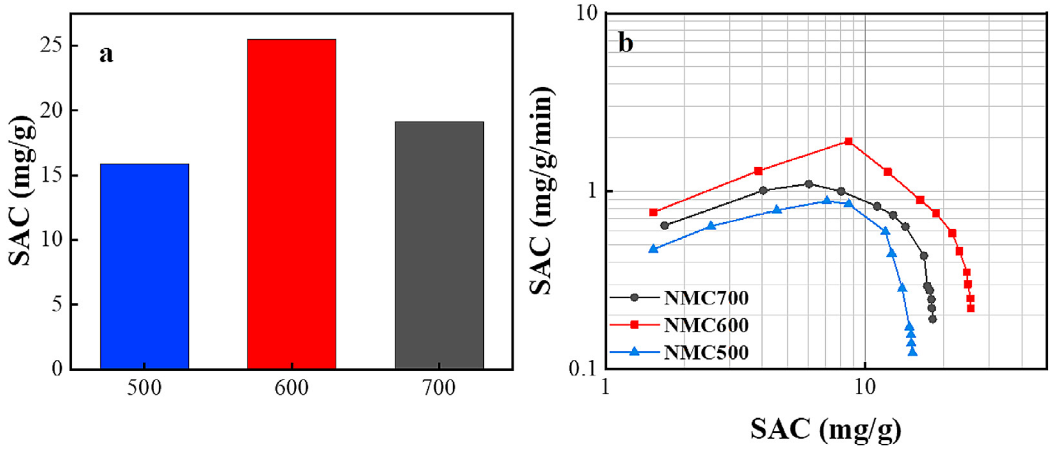

Fig. 8 – (a) Electrosorption capacities of NMC500, NMC600, and NMC700 electrodes and (b) Ragone plots of NMC500, NMC600, and NMC700 electrodes

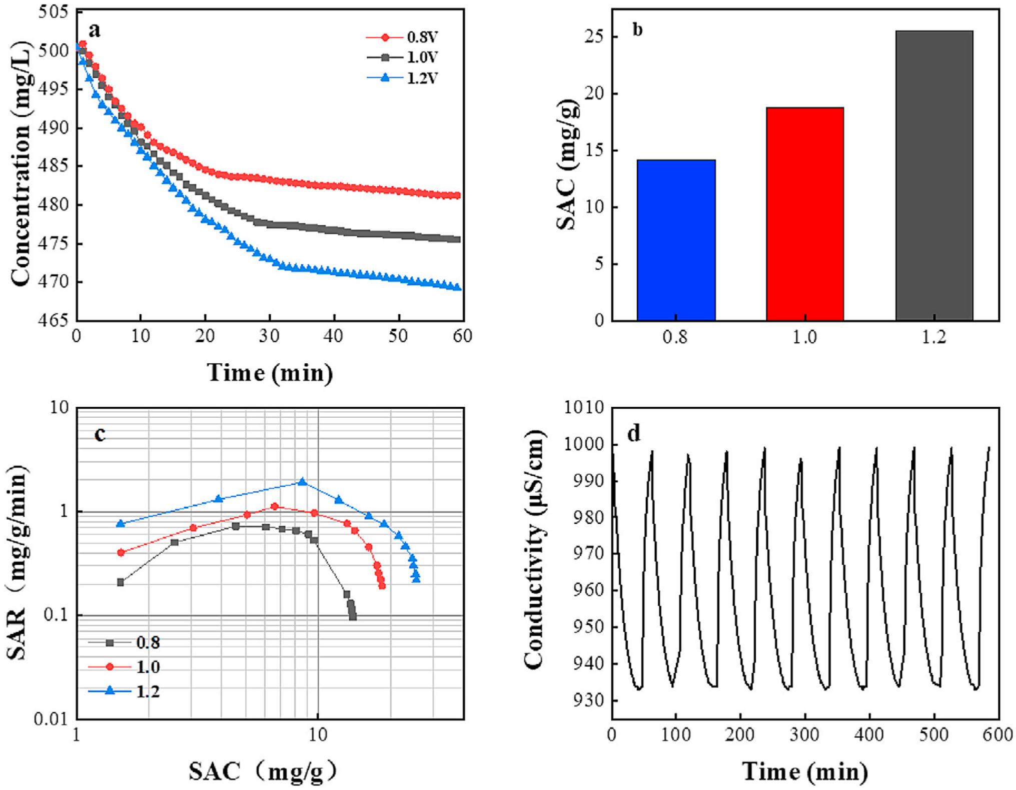

Fig. 9 – (a) Changes in the circulating solution concentration with time, (b) electrosorption capacity of NMC600 at various voltages, (c) Ragone plots of NMC600 at various voltages, and (d) cycling desalination performance of NMC600.

a rich nitrogen content that promotes electrical conductivity and wettability are key factors enabling NMC600 electrodes to achieve the best deionization performance in the CDI test. The energy consumption and charge efficiency of each material is summarized in Table 2. Compared with the NMC500 and NMC700 electrodes, the NMC600 electrode exhibited the highest charge utilization and lowest energy consumption. These results verify the importance of the balance between the pore structure and nitrogen content in the electrode material for CDI.

Table 2 – Comparison of charge efficiency and energy consumption of NMC500, NMC 600, and NMC700.

Sample	Charge efficiency	Energy consumption (kWh/kg)
NMC500	0.50	0.82
NMC600	0.58	0.75
NMC700	0.53	0.79

To examine the SAC of the NMC600, CDI experiments were conducted under voltages of 0.8, 1.0, and 1.2 V (Fig. 9a–c). The solution concentration initially increased sharply and reached a stable state within 60 min. The SAC also increased from 14.48 to 25.53 mg/g with increasing voltage (Fig. 9b). Thus, a higher voltage results in a higher SAC because of the stronger electrostatic interactions. Water hydrolysis was not observed during the experimental process because of the intrinsic resistance in the circuit. Fig. 9c shows the electrosorption rates at different voltages. Further, with increasing voltage, the curve shifts to the right, indicating that the SAC and SAR increase simultaneously owing to the easy adsorption of ions caused by stronger Coulombic interactions at higher voltages (Andelman, 2011).

Cycling stability can be evaluated using adsorption–regeneration experiments. Fig. 9d shows the cyclic absorption/desorption experiments performed on the NMC600 electrode under 1.2 V. The adsorption and desorption processes were completed quickly during regeneration, indicating an excellent regeneration ability. After 10 cycles, although the adsorption time of the NMC600 slightly increased, there was very little degradation, indicating its high potential for practical use in CDI. In addition, Appendix A Fig. S4 shows the SEM results of the NMC samples after multiple adsorption-desorption cycles, revealing that the pore structure was not destroyed after the operation. This implies the good stability of the materials. Compared with CDI electrodes synthesized by other methods (Appendix A Table S3), NMC600 showed a good electrosorption capacity, which suggests that the nitrogen-rich micro-mesoporous carbons obtained via a simple strategy exhibit excellent CDI performance.

3. Conclusions

In this study, we prepared NMC CDI electrodes by directly carbonizing an SNW-1. The results showed that, because of its large surface area (312 m^2/g) and optimal chemical composition (15.57% of nitrogen content), NMC600 showed a high specific capacitance (152.33 F/g) and the best SAC (25.53 mg/g). This indicates the importance of the balance between pore structure and chemical composition for CDI performance. In addition, the NMC600 showed excellent electrosorption stability in the recycling experiment. These findings indicate the promising potential of POF-driven carbon materials for desalination by CDI.

Acknowledgments

This work was supported by the Local Innovative and Research Teams Project of Guangdong Pearl River Talents Program (No. 2017BT01Z032), the National Natural Science Foundation of China (No. 21577027), the 2017 Central Special Fund for Soil, Preliminary Study on Harmless Treatment and Comprehensive Utilization of Tailings in Dabao Mountain (No. 18HK0108).

Appendix A Supplementary data

Supplementary material associated with this article can be found, in the online version, at doi:10.1016/j.jes.2021.03.006.

REFERENCES

Andelman, M., 2011. Flow through capacitor basics. Sep. Purif. Technol. 80, 262–269.

Anderson, M.A., Cudero, A.L., Palma, J., 2010. Capacitive deionization as an electrochemical means of saving energy and delivering clean water. Comparison to present desalination practices: will it compete? Electrochim. Acta 55, 3845–3856.

Kim, D.J., Yoon, J.W., Lee, C.S., Bae, Y.S., Kim, J.H., 2018. Covalent organic framework-derived microporous carbon nanoparticles coated with conducting polypyrrole as an electrochemical capacitor. Appl. Surf. Sci. 439, 833–838.

Li, D., Ning, X.an, Huang, Y., Li, S., 2019. Nitrogen-rich microporous carbon materials for high-performance membrane capacitive deionization. Electrochim. Acta 312, 251–262.

Liu, D., Ning, X.an, Hong, Y., Li, Y., Bian, Q., Zhang, J., 2019. Covalent triazine-based frameworks as electrodes for high-performance membrane capacitive deionization. Electrochim. Acta 296, 327–334.

Ma, J., Cheng, Y., Wang, L., Dai, X., Yu, F., 2020. Free-standing Ti3C2Tx MXene film as binder-free electrode in capacitive deionization with an ultrahigh desalination capacity. Chem. Eng. J. 384, 123329.

Pastushok, O., Zhao, F., Ramasamy, D.L., Sillanpää, M., 2019. Nitrate removal and recovery by capacitive deionization (CDI). Chem. Eng. J. 375, 121943.

Semiat, R., 2008. Energy issues in desalination processes. Environ. Sci. Technol. 42, 8193–8201.

Shi, P., Wang, C., Sun, J., Lin, P., Xu, X., Yang, T., 2020. Thermal conversion of polypyrrole nanotubes to nitrogen-doped carbon nanotubes for efficient water desalination using membrane capacitive deionization. Sep. Purif. Technol. 235, 116196.

Shunmughanathan, M., Puthiaraj, P., Pitchumani, K., 2015. Melamine-based microporous network polymer supported palladium nanoparticles: a stable and efficient catalyst for the sonogashira coupling reaction in water. ChemCatChem 7, 666–673.

Singh, K., Qian, Z., Biesheuvel, P.M., Zuilhof, H., Porada, S., de Smet, L.C.P.M., 2020. Nickel hexacyanoferrate electrodes for high mono/divalent ion-selectivity in capacitive deionization. Desalination 481, 114346.

Song, Y., Hu, J., Liu, J., Evrendilek, F., Buyukada, M., 2020. Catalytic effects of CaO, Al_2O_3, Fe_2O_3, and red mud on Pteris vittata combustion: emission, kinetic and ash conversion patterns. J. Clean. Prod. 252, 119646.

Wang, P., Wu, Q., Han, L., Wang, S., Fang, S., Zhang, Z., et al., 2015. Synthesis of conjugated covalent organic frameworks/graphene composite for supercapacitor electrodes. RSC Adv. 5, 27290–27294.

Wang, Z., Yan, T., Fang, J., Shi, L., Zhang, D., 2016. Nitrogen-doped porous carbon derived from a bimetallic metal-organic framework as highly efficient electrodes for flow-through deionization capacitors. J. Mater. Chem. A 4, 10858–10868.

Wei, Y., Huo, Y., Tian, G., Meng, Q., Cao, B., 2016. Nitrogen-doped functional graphene nanocomposites for capacitive deionization of NaCl aqueous solutions. J. Solid State Electrochem. 20, 2351–2362.

Zhao, S., Yan, T., Wang, H., Chen, G., Huang, L., Zhang, J., et al., 2016. High capacity and high rate capability of nitrogen-doped porous hollow carbon spheres for capacitive deionization. Appl. Surf. Sci. 369, 460–469.

Zhao, X., Yan, N., 2015. One-pot synthesis and assembly of melamine-based nanoparticles for microporous polymer organic frameworks and their application as a support for a silver nanoparticle catalyst. RSC Adv. 5, 69955–69961.

Zhu, G., Wang, H., Xu, H., Zhang, L., 2018. Enhanced capacitive deionization by nitrogen-doped porous carbon nanofiber aerogel derived from bacterial-cellulose. J. Electroanal. Chem. 822, 81–88.